Proceedings of the Thirty-sixth (2026) International Ocean and Polar Engineering Conference
Orlando, Florida, USA, May 31-June 5, 2026

ISBN 978-1-880653-72-2; ISSN 1098-6189
www.isope.org

Suppression of Internal Solitary Wave-Induced Depth Drop in Submarines via PD–PI Autopilot Control

Linjie Li[1], Qingjie Meng[2], Liushuai Cao[1], Decheng Wan[1]*

[1] Computational Marine Hydrodynamics Lab (CMHL), School of Ocean and Civil Engineering,
Shanghai Jiao Tong University, Shanghai, China
[2] Wuhan Second Ship Design and Research Institute, Wuhan, China
[*]Corresponding author

ABSTRACT

Internal solitary waves can significantly impair the depth keeping performance of underwater vehicles. This study develops a numerical wave tank based on the eKdV equation to investigate the motion response and control of a self-propelled submarine encountering an ISW. Fully coupled simulations of hull motion, propeller rotation, and control surface deflection are achieved using overset and sliding mesh techniques. The results show that PD control of the stern rudder reduces the maximum depth drop to 33% of the uncontrolled case, while a combined PI–PD control strategy, in which PI control adjusts the propeller rotational speed, further decreases it to 17%.

KEY WORDS: Internal solitary wave; Submarine; PD control; PI control; Motion response; Self-propelled.

INTRODUCTION

In the ocean, stable density stratification commonly forms due to temperature and salinity variations, giving rise to internal waves when disturbed (Cao et al., 2024). Among them, internal solitary waves (ISWs) are characterized by large amplitudes, high energy, and predominant occurrence in deep waters, which makes their prediction and real-time monitoring particularly challenging (Helfrich and Melville, 2006). As a result, submarines often lack sufficient time to implement effective evasive maneuvers once an ISW encounter is detected (Gong et al., 2022). The South China Sea is one of the most active regions for ISWs worldwide (Alford et al., 2015), highlighting the engineering importance of submarine motion responses under such conditions.

A variety of theoretical models have been developed to describe ISWs. The applicability of these models depends largely on the degree of nonlinearity and dispersion of the wave field (Cui et al., 2021). In general, weakly nonlinear ISWs can be described by the KdV equation, while large-amplitude or strongly nonlinear waves require more advanced models such as eKdV, mKdV, MCC, DJL, or HLGN theories (Benjamin, 1966; Lee and Beardsley, 1974; Michallet and Barthelemy, 1998; Choi and Camassa, 1999; Dunphy et al., 2011; Zhao et al., 2016).

Given that ISW wavelengths are typically much larger than the characteristic length of underwater vehicles, the feedback of the vehicle on the ambient wave field is often neglected. Under this assumption, hydrodynamic loads have been extensively investigated using internal wave theories combined with the Morison equation. Early studies focused on idealized geometries such as vertical or slender cylinders (Cai et al., 2003, 2006, 2008), while later works improved load prediction accuracy by incorporating nonlinear effects or adopting eKdV based formulations validated by laboratory experiments (Zan and Lin, 2020, 2021; Xuan et al., 2023). However, these semi-empirical approaches are limited in their ability to resolve detailed flow structures.

Experimental studies have further explored ISW-induced loads and motions of submerged bodies. Investigations on fixed or floating models revealed strong dependencies on wave amplitude, submergence depth, orientation, and proximity to the pycnocline (Wei et al., 2014; Cui et al. 2019, 2020; Wang et al., 2020; Xuan et al., 2024). Although experiments provide valuable physical insight, their high cost and limited flow field accessibility restrict their applicability for comprehensive parametric analyses.

With advances in high-performance computing, CFD has become a powerful tool for studying ISW–structure interactions. Recent numerical studies have examined the effects of wave amplitude, submergence depth, forward speed, and incidence angle on the hydrodynamic loads and motion responses of underwater vehicles, particularly using the SUBOFF model (Ding et al., 2023; Huang et al., 2023; Cheng et al., 2024a; He et al., 2024). Nevertheless, these investigations focus on passive responses, without considering active control strategies.

Only limited attempts have been made to introduce control concepts into ISW-related studies. Cheng et al. (2023, 2024b) applied a PD controller by adding corrective moments to the equations of motion, achieving partial suppression of ISW-induced heave and pitch motions. However, this approach does not reflect realistic submarine operations, where control moments are generated through hydrodynamic forces acting on control surfaces.

In contrast, submarine control systems have been extensively studied in calm water and surface wave environments. Autopilot-based simulations incorporating overset mesh, sliding mesh, and six-degree-of-freedom motion have demonstrated the effectiveness of stern planes and sail planes in maneuvering and depth control (Carrica et al., 2019; Han et al., 2021; Chen et al., 2023; Guo et al., 2024). Despite these advances, the influence of ISWs on submarine control performance has not yet been addressed.

Based on the above review, it is evident that existing studies on ISWs have primarily focused on hydrodynamic characteristics and passive motion responses, while research on submarine control has largely neglected ISW environments. Consequently, the control mechanisms of submarines encountering ISWs remain unclear. Addressing this gap constitutes the main motivation of the present study. The remainder of this paper is organized as follows: Section 2 introduces the numerical methodology; Section 3 presents the numerical setup and validation; Section 4 discusses the motion responses and control effectiveness; and Section 5 summarizes the main conclusions.

METHODOLOGY

Governing Equations

The numerical simulations were performed using the commercial CFD package STAR-CCM+. The flow field was resolved by solving the Reynolds-averaged Navier–Stokes (RANS) equations. The governing equations consist of the continuity equation and the momentum conservation equations, which can be written as follows:

$$\frac{\partial \overline{u}_i}{\partial x_i} = 0 \tag{1}$$

$$\frac{\partial \overline{u}_i}{\partial t} + \overline{u}_j \frac{\partial \overline{u}_i}{\partial x_j} = -\frac{1}{\rho}\frac{\partial \overline{p}}{\partial x_i} + \nu \frac{\partial^2 \overline{u}_i}{\partial x_j^2} - \frac{\partial \overline{u_i' u_j'}}{\partial x_j} + \overline{f}_i \tag{2}$$

where $\overline{u}_i$ denotes the time-averaged velocity component, $\overline{u_i' u_j'}$ represents the Reynolds stress term, and $\overline{p}$ and $\overline{f}_i$ are the time-averaged pressure and body force, respectively.

Turbulence Model

The SST k–ω turbulence model is employed to provide closure for the RANS equations. It retains the robustness of the k–ω model near walls and incorporates the $k-\varepsilon$ behavior in the outer flow. The governing transport equations for $k$and $\omega$are expressed as follows (Menter, 1994):

$$\frac{\partial(\rho k)}{\partial t} + \frac{\partial(\rho k u_i)}{\partial x_i} = \frac{\partial}{\partial x_j}\left(\Gamma_k \frac{\partial k}{\partial x_j}\right) + G_k - Y_k + S_k \tag{3}$$

$$\frac{\partial(\rho \omega)}{\partial t} + \frac{\partial(\rho \omega u_i)}{\partial x_i} = \frac{\partial}{\partial x_j}\left(\Gamma_\omega \frac{\partial \omega}{\partial x_j}\right) + G_\omega - Y_\omega + S_\omega \tag{4}$$

where Γ_k and Γ_ω are the effective diffusivities, G_k and G_ω are the production terms, Y_k and Y_ω represent dissipation due to turbulence, and S_k and S_ω denote source terms.

Volume of Fluid Method

The VOF technique (Hirt and Nichols, 1981) is employed to describe the interface between two immiscible fluid layers involved in the propagation of internal solitary waves. The interface location is determined from the local volume fraction of each phase in the computational domain.

$$\frac{\partial r}{\partial t} + \frac{\partial}{\partial x_i}(r\overline{u}_i) = 0 \tag{5}$$

$$r^{(k)} = V^{(k)} / \sum_{k=1}^{n} V^{(k)} \tag{6}$$

A HRIC scheme is applied in STAR-CCM+ to ensure a sharp phase interface. The interface is associated with cells where $0 < r < 1$, and the ISW profile is extracted from the iso-surface corresponding to a volume fraction of 0.5 for the upper fluid.

Theoretical Model for ISW

To model internal solitary waves, a numerical wave tank based on the eKdV theory is employed in this study. The evolution of the interfacial displacement follows the eKdV equation, given by:

$$\frac{\partial \eta}{\partial t} + (c_0 + c_1\eta + c_3\eta^2)\frac{\partial \eta}{\partial x} + c_2\frac{\partial^3 \eta}{\partial x^3} = 0 \tag{7}$$

$$c_0^2 = \frac{g h_1 h_2 (\rho_1 - \rho_2)}{\rho_1 h_2 + \rho_2 h_1} \tag{8}$$

$$c_1 = -\frac{3c_0}{2}\frac{\rho_1 h_2^2 - \rho_2 h_1^2}{\rho_1 h_1 h_2^2 + \rho_2 h_1^2 h_2} \tag{9}$$

$$c_2 = \frac{c_0}{6}\frac{\rho_2 h_1 h_2^2 + \rho_1 h_1^2 h_2}{\rho_1 h_2 + \rho_2 h_1} \tag{10}$$

$$c_3 = \frac{3c_0}{h_1^2 h_2^2}\left[\frac{7}{8}\left(\frac{\rho_1 h_2^2 - \rho_2 h_1^2}{\rho_1 h_2 + \rho_2 h_1}\right)^2 - \frac{\rho_1 h_2^3 + \rho_2 h_1^3}{\rho_1 h_2 + \rho_2 h_1}\right] \tag{11}$$

where η is the ISW profile, and ρ_i and h_i $(i = 1,2)$ denote the density and layer depth of the upper and lower fluids.

An analytical expression for η is given by:

$$\eta(x,t) = \frac{\eta_0}{B + (1-B)cosh^2\left(\frac{x - c_{eKdV}t}{l_{eKdV}}\right)} \tag{12}$$

$$c_{\text{eKdV}} = c_0 + \frac{\eta_0}{3}\left(c_1 + \frac{1}{2}c_3\eta_0\right) \tag{13}$$

$$l_{\text{eKdV}} = \sqrt{\frac{12c_2}{\left(c_1 + \frac{1}{2}c_3\eta_0\right)\eta_0}} \tag{14}$$

$$B = \frac{-c_3\eta_0}{2c_1 + c_3\eta_0} \tag{15}$$

where η_0 is the wave amplitude, c_{eKdV} denotes the theoretical phase velocity, l_{eKdV} is the characteristic wavelength, and B is an auxiliary parameter.

The inlet boundary condition for the velocity field is imposed using a user-defined function (UDF), which can be written as:

$$U(t) = \begin{cases} -c_{\text{eKdV}}\dfrac{\eta(x,t)}{h_1 - \eta(x,t)}, & z > \eta(x,t) \\ c_{\text{eKdV}}\dfrac{\eta(x,t)}{h_2 + \eta(x,t)}, & z < \eta(x,t) \end{cases} \tag{16}$$

COMPUTATIONAL SETUP AND VALIDATIONS

The Joubert BB2 Submarine Model

Table 1. Main parameters of the Joubert BB2 (model scale 1:18.348).

Description	Symbol	Model
Overall length	L (m)	3.826
Beam	B (m)	0.523
Draft to deck	D_d (m)	0.578
Draft to sail top	D_s (m)	0.883
Diameter of propeller	D_p (m)	0.273
Displacement	∇ ($tons$)	0.7012
Longitudinal Center of Gravity	X_{CG} (m)	1.761
Vertical Center of Gravity	Z_{CG} (m)	0.0024
X-axis Moment of Inertia	I_{xx} ($kg{\cdot}m^2$)	30.849
Y-axis Moment of Inertia	I_{yy} ($kg{\cdot}m^2$)	665.448
Z-axis Moment of Inertia	I_{zz} ($kg{\cdot}m^2$)	665.229

A fully appended Joubert BB2 submarine is adopted as the geometric model. The hull form, developed by Joubert and later modified by MARIN, incorporates the hull, sail, sail planes, and X-rudders, and is equipped with a six-bladed MARIN 7371R propeller. The geometry and principal parameters are presented in Fig. 1 and Table 1, respectively.

Fig. 1 The Joubert BB2 geometry.

Computational Domain and Mesh Configuration

An overset mesh strategy is used to simulate submarine motions under an ISW. The domain comprises a background region for the ISW flow and a near field overset region for submarine motion, coupled via overset interfaces. Propeller rotation is modeled using a sliding mesh, while the independent motions of the four rudders are handled through the overset mesh method, as shown in Fig. 2.

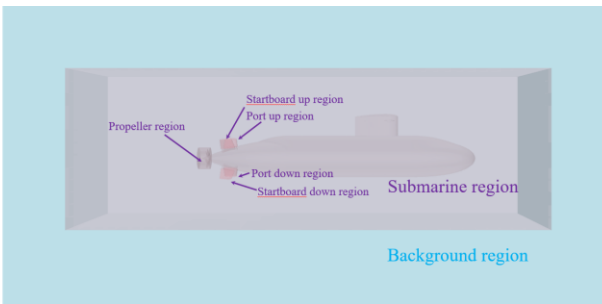

Fig. 2 The overset regions.

The domain is meshed using trimmed cells, with local refinements in the ISW region and near the propeller and rudders, as shown in Fig. 3. Prism layers are applied on the submarine surface to resolve the boundary layer. The final mesh consists of approximately 16 million cells.

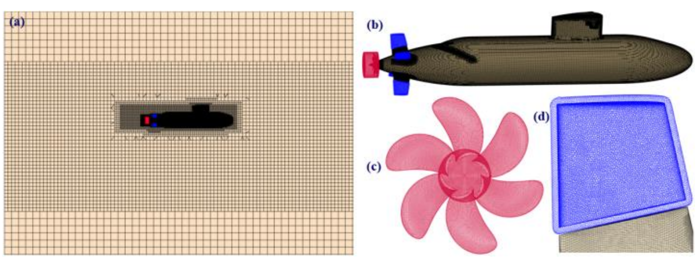

Fig. 3 Computational mesh configuration: (a) mesh on the $y = 0$ plane; (b) submarine mesh; (c) propeller surface mesh; (d) rudder mesh.

Boundary Conditions

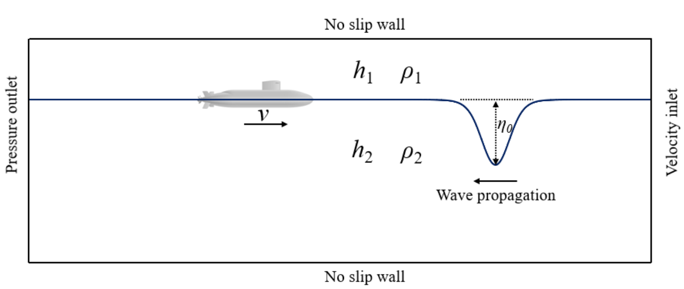

Fig. 4 Schematic diagram of the numerical tank with submarine.

The numerical wave tank configuration is shown in Fig. 4. The domain size is 300 m × 15 m × 25 m, with a two-layer stratification of 5 m and 20 m depth, where the densities of the upper and lower layers are 998 kg/m³ and 1025 kg/m³, respectively. Boundary conditions include a velocity inlet, pressure outlet, no slip walls, and symmetry planes. A 4 m amplitude ISW is generated at the inlet. It should be clarified that for the 4 m wave amplitude considered in this study, the eKdV theory provides sufficient accuracy. However, when the wave amplitude increases to extreme values, such as 6 m or larger, the eKdV theory becomes invalid, and the mKdV theory should be employed instead. The submarine initially rests at the density interface and moves opposite to ISW propagation, with its motion released when the distance between the center of mass and the ISW trough reaches 90 m.

Autopilot Control

The propeller speed is regulated by a PI controller to achieve self-propulsion, with the control law minimizing the velocity error between the target and actual submarine speeds. The governing equation is provided in Eq. 17 (Carrica et al., 2019).

$$R(t) = R_0(1 + K_p \cdot \text{error} + K_i \cdot \sum \text{error}) \tag{17}$$

where $R(t)$ is the instantaneous propeller speed, R_0 is the initial speed, and the error is the difference between the target and actual submarine velocities. The gains K_p and K_i are the proportional and integral coefficients.

The PI-based thrust regulation strategy proposed in this study for abrupt flow variations induced by internal solitary waves is conceptually similar to the Dynamic Positioning strategy adopted by vessels navigating in brash ice conditions in polar engineering. In both types of extreme marine environments, the propulsion system is required to respond rapidly and effectively to sudden changes in external hydrodynamic loads.

Stern rudders are used to control the submarine attitude. Only equivalent diving planes are considered for vertical-plane motion, while yaw control is excluded. Since X-rudder deflections are not intuitively decoupled, a conversion model is required to relate the X-rudder angles to the equivalent cruciform rudder angles, as given in Eqs. 18~19.

$$\delta_1 = \delta_3 = -\delta_s \tag{18}$$

$$\delta_2 = \delta_4 = \delta_s \tag{19}$$

where δ_s is the effective stern plane angle, and $\delta_1 - \delta_4$ denote the deflection angles of the four X-rudders, as shown in Fig. 5, defined from the stern-to-bow viewpoint.

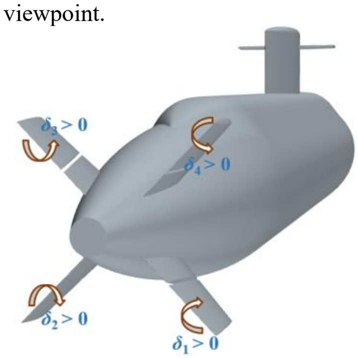

Fig. 5 The X-rudders of Joubert BB2 submarine.

A PD controller is employed to achieve real-time automatic control of the rudder angles and stabilize the vertical-plane motion of the Joubert BB2 submarine (Overpelt, et al., 2015). The control law is defined in Eqs. 20.

$$\delta_s(t) = P_z e(t) + D_z \frac{de(t)}{dt} + P_\theta e(t) + D_\theta \frac{de(t)}{dt} \tag{20}$$

Where, P_z is 55.4 degrees/m, D_z is −12.85 degrees/(m/s), P_θ is 3 degrees/degree, and D_θ is 0.7 degrees/(degree/s).

Verification and Validation

Owing to the lack of experimental data for self-propelled submarines operating in ISW environments, a two-stage validation approach is employed. First, the accuracy of the self-propulsion simulation in calm water is assessed. Second, the predicted motion response of a suspended structure under ISW conditions is validated.

Table 2. Mesh convergence results for the self-propelled condition.

Mesh case	Cells (million)	Thrust (N)	Rotational speed (rpm)
1	5.7	27.08	282
2	12	27.71	285.5
3	16	29.05	288.4
4	26	28.54	287.1

For the calm-water case, a grid convergence study is carried out in deep, still water at a speed of 1.2 m/s, with a fluid density of 997.561 kg/m³. Four mesh resolutions with 5.7, 12, 16, and 26 million cells are considered. All meshes employ the same local refinement strategy, differing only in the base mesh size. The propeller speeds obtained from the PI controller and the corresponding thrust at self-propulsion are listed in Table 2.

To ensure statistical soundness, a grid uncertainty analysis was performed based on the Grid Convergence Index (GCI) method (Celik et al., 2008). Considering the oscillatory convergence behavior observed among the refined meshes, the theoretical apparent order of the spatial discretization ($p = 2$) was adopted with a safety factor of $F_s = 1.25$. Using the finest mesh (26 million) as the reference, the refinement ratio for the selected 16 million-cell mesh is $r = 1.176$. The calculated GCI values for the 16 million-cell mesh are 5.85% for thrust and 1.47% for rotational speed. These low numerical uncertainties indicate that the spatial discretization error is well controlled, and it does not affect the physical claims regarding the submarine motion responses presented in this study.

The self-propulsion results obtained using Mesh case 3 are further validated by comparison with deep-water experimental data from Overpelt (2015), as shown in Table 3.

Table 3. Results of CFD and experiments under self-propulsion condition.

Parameters	Experiment	Present	Error
Rotating speed (rpm)	268	272	1.49%
Thrust (N)	26.6	24.92	-6.32%

As shown in Table 3, the numerical predictions agree well with the experimental data, with a rotational speed error of 1.49% and a thrust difference within 7%, demonstrating the reliability of the self-propulsion simulation method.

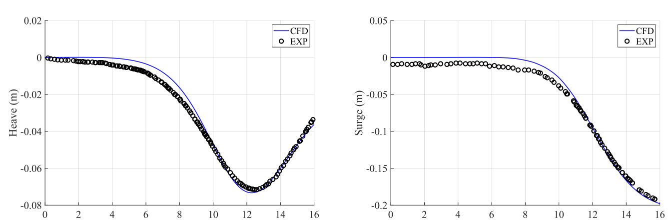

(a) Heave motion (b) Surge motion

Fig. 6 Comparison of sphere motion responses in ISW.

To validate the ISW-induced motion response, a numerical simulation of a suspended sphere was performed and compared with the experimental results of Cui et al. (2020). The upper and lower layer depths are 0.1 m and 0.4 m, with densities of 1030 and 1051 kg/m³, respectively. The ISW amplitude is 0.0827 m, and a sphere with a diameter of 0.088 m is initially located 0.05 m below the density interface. Several previous studies about ISW-submarine interaction have also adopted the motion trajectory of the spherical model for validation (Cheng et al., 2023; Cheng et al., 2024a). The numerical method employed in the present study is physically consistent with those published benchmark cases.

As shown in Fig. 6, the numerical predictions of heave and surge motions agree well with the experimental measurements in both peak response and overall trend, confirming the validity of the numerical model.

RESULTS AND DISCUSSION

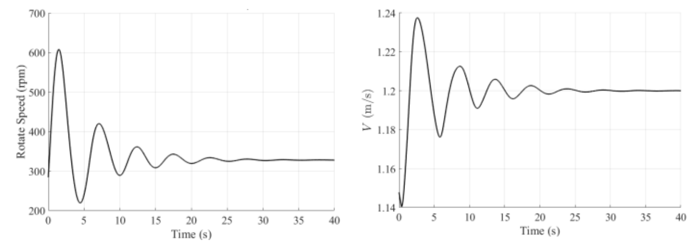

(a) Rotational speed (b) Velocity

Fig. 7 Propeller rotational speed and submarine velocity during self-propulsion in a still water environment.

Under still stratified conditions (ISW amplitude equals zero), a PI controller is used to determine the propeller speed required for a self-propulsion velocity of 1.2 m/s, with $R_0 = 272$ rpm, $K_p = 1$, and $K_i = 0.2$. It should be clarified that these parameters were derived from previous self-propulsion results obtained under calm-water conditions (Guo et al., 2024), and no further adjustment of this parameter was performed in the present study. Figure 7 illustrates the time histories of the propeller rotational speed and submarine velocity under still water self-propulsion condition, the results indicate that the propeller rotational speed at the self-propulsion point is 324 rpm.

Three control modes are examined to evaluate the submarine motion response to an ISW: constant rotational speed without stern rudder control, constant rotational speed with PD-controlled stern rudder, and PI-regulated variable rotational speed with PD-controlled stern rudder. The corresponding simulation cases are listed in Table 4.

Table 4. Control parameters of propeller rotational speed and stern rudder for the 3 cases.

Case	Propeller rotational speed (rpm)	Stern rudder control
1	324	No
2	324	PD
3	PI	PD

Motion Response of the Submarine under ISW

For a submarine cruising at 1.2 m/s and initially placed at the interface, the motion displacements over time are summarized in Fig. 8, while Fig. 9 depicts its spatial evolution under three different control strategies during successive stages of ISW interaction.

The displacement time histories in Fig. 8 further reveal the differences among the control strategies. For the surge motion, the displacement curve in Case 3 exhibits a linear growth trend, indicating that the submarine successfully maintains its target cruising speed. In contrast, for Cases 1 and 2, the slope of the curves decreases significantly after $t = 120$s. In terms of pitch motion, the maximum bow-up angles in Cases 1 and 2 exceed 15°, whereas in Case 3 the maximum bow-up angle is limited to within 10° and rapidly recovers to near 0°.

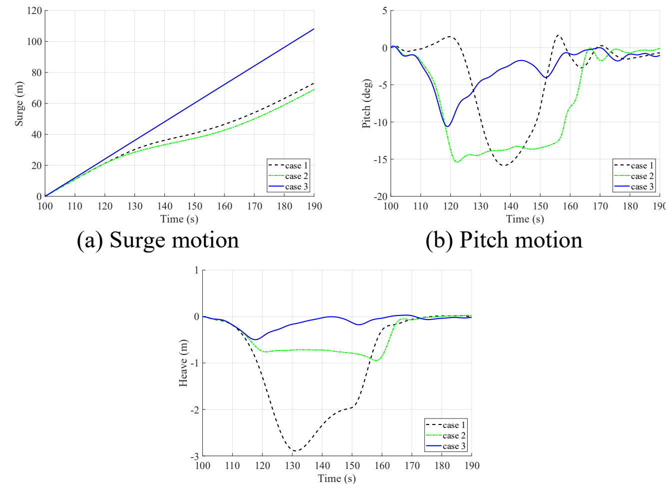

(a) Surge motion (b) Pitch motion

(c) Heave motion

Fig. 8 Trajectory of a self-propelled submarine under an ISW.

Regarding the heave motion, under the influence of the ISW, the maximum sinking depth in Case 1 reaches 2.89 m. In Case 2, although stern rudder control is applied, the maximum sinking depth is still 0.94 m, and the submarine remains at a depth approximately 0.72 m below its initial position for an extended period during the internal solitary wave. In contrast, only Case 3, through the combined control strategy of propeller rotational speed and stern rudder angle, successfully limits the maximum sinking depth to within 0.5 m and enables a rapid recovery to near the initial position.

To propagate the calm-water numerical uncertainties discussed in the previous section to the key motion responses under ISW conditions, a linear error-propagation estimation is adopted. By conservatively assuming that the uncertainty in the predicted thrust translates proportionally to the resulting depth variation, the maximum GCI of 5.85 % is applied to the maximum depth drops of the three operational cases. For the uncontrolled submarine (Case 1), this corresponds to an absolute uncertainty of approximately ±0.17 m for the 2.89 m maximum depth drop. For the PD-controlled scenario (Case 2), the estimated uncertainty is about ±0.05 m for the 0.94 m depth drop. Finally, for the fully combined PI–PD control case (Case 3), the uncertainty is only ±0.03 m for the 0.50 m depth drop. Because the resulting error bands for the three cases (2.72~3.06 m, 0.89~0.99 m, and 0.47~0.53 m, respectively) are well separated and non-overlapping, the propagated numerical uncertainties are considered negligible. This confirms that the numerical uncertainties do not affect the physical conclusions regarding the hierarchical effectiveness of the control strategies.

Figure 9 intuitively illustrates the relative position of the submarine as it encounters the internal wave. A comparison of the three cases reveals distinct behaviors. In Case 1, due to the absence of stern rudder control, the submarine exhibits a passive drifting motion. In Case 2, although a PD controller is employed to control the stern rudder for depth keeping, the submarine still experiences sinking after entering the internal solitary wave and maintains a bow-up attitude throughout. In contrast, in Case 3, the combination of a PI-regulated propeller and a PD-controlled stern rudder effectively alleviates the sinking tendency of the submarine after encountering the internal wave, thereby maintaining the most stable attitude among the three cases.

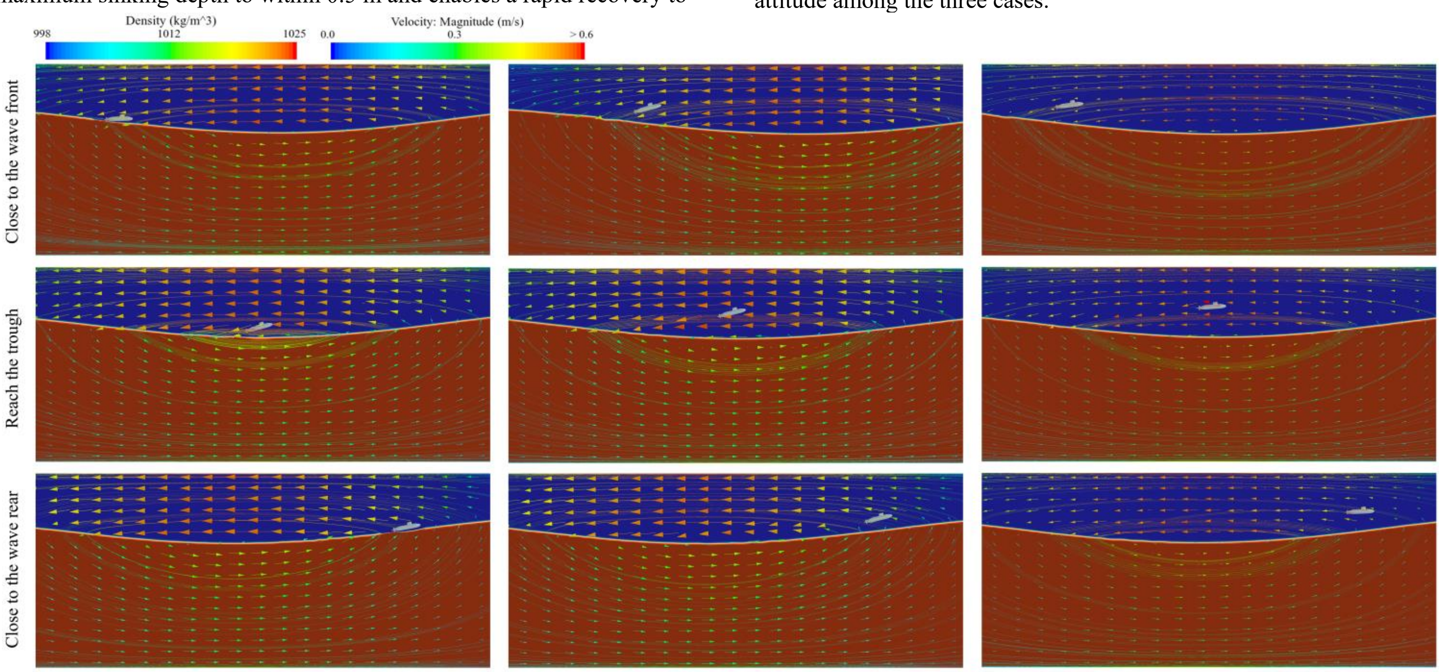

（1） case 1 （2） case 2 （3） case 3

Fig. 9 Wave profiles and relative positions of a self-propelled submarine during three stages of encountering an ISW.

Horizontal Velocity

This section focuses on the evolution of the horizontal velocity field during ISW interaction. The associated velocity time histories are given in Fig. 10, while the horizontal wake patterns under three control strategies at key ISW stages are shown in Fig. 11.

As shown in Fig. 10, Case 3 demonstrates an exceptionally stable speed-keeping capability. Throughout the entire encounter with the wave-induced disturbance, the velocity remains nearly constant at approximately 1.2 m/s. In contrast, in Cases 1 and 2, the submarine experiences a pronounced drop in speed upon encountering the internal solitary wave, with the minimum velocity decreasing to about 0.4 m/s. Moreover, in Case 2, the activation of the PD-controlled stern rudder introduces additional hydrodynamic resistance during depth correction, resulting in a lower velocity than that observed in Case 1.

From the horizontal velocity field in Fig.11, a long and narrow dark-blue wake region can be observed downstream of the submarine stern in Case 3. This feature provides direct evidence that, after the PI controller detects the adverse velocity field encountered by the submarine and the associated reduction in forward speed, it rapidly increases the propeller rotational speed, thereby generating a strong thrust jet. In contrast, the wakes in Cases 1 and 2 are much shorter, indicating lower kinetic energy levels.

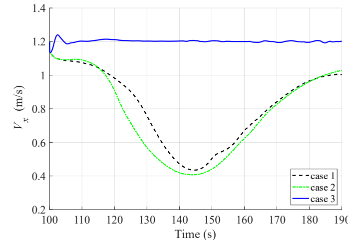

Fig. 10 Horizontal velocity of the submarine.

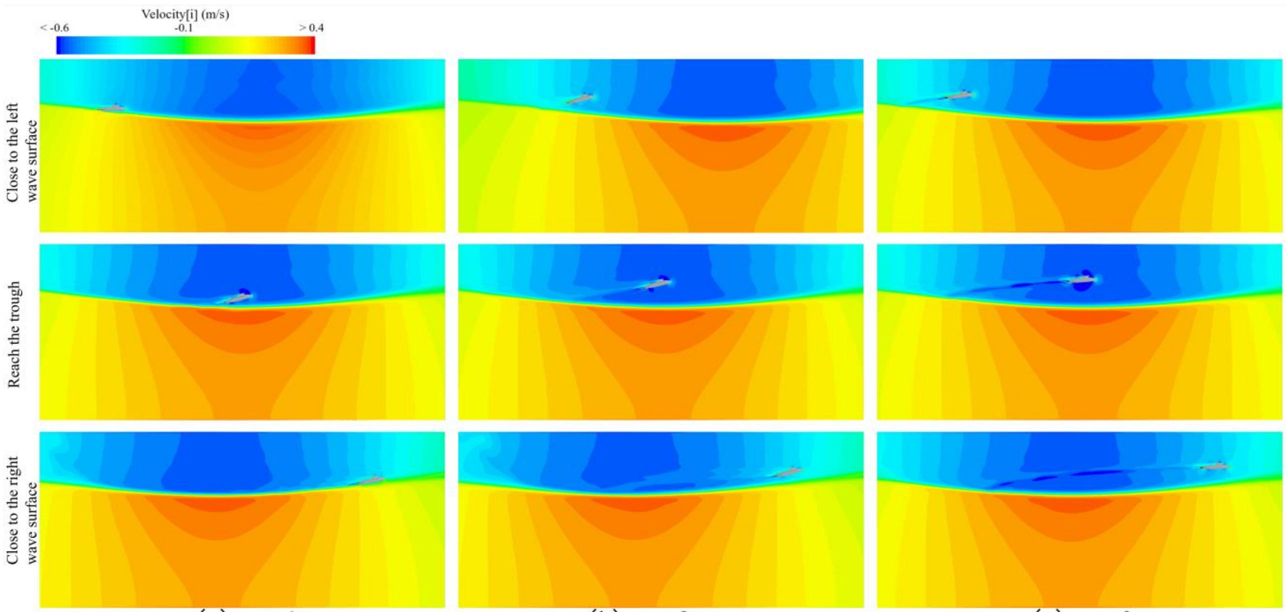

（a） case 1 （b） case 2 （c） case 3

Fig. 11. Horizontal velocity field at three representative stages of ISW–submarine interaction.

Vertical Velocity

This section addresses the vertical velocity field evolution during the interaction between ISW and submarine. Figure 12 shows the vertical velocity distributions at key stages for the three control strategies, while Fig. 13 presents the submarine vertical velocity time histories.

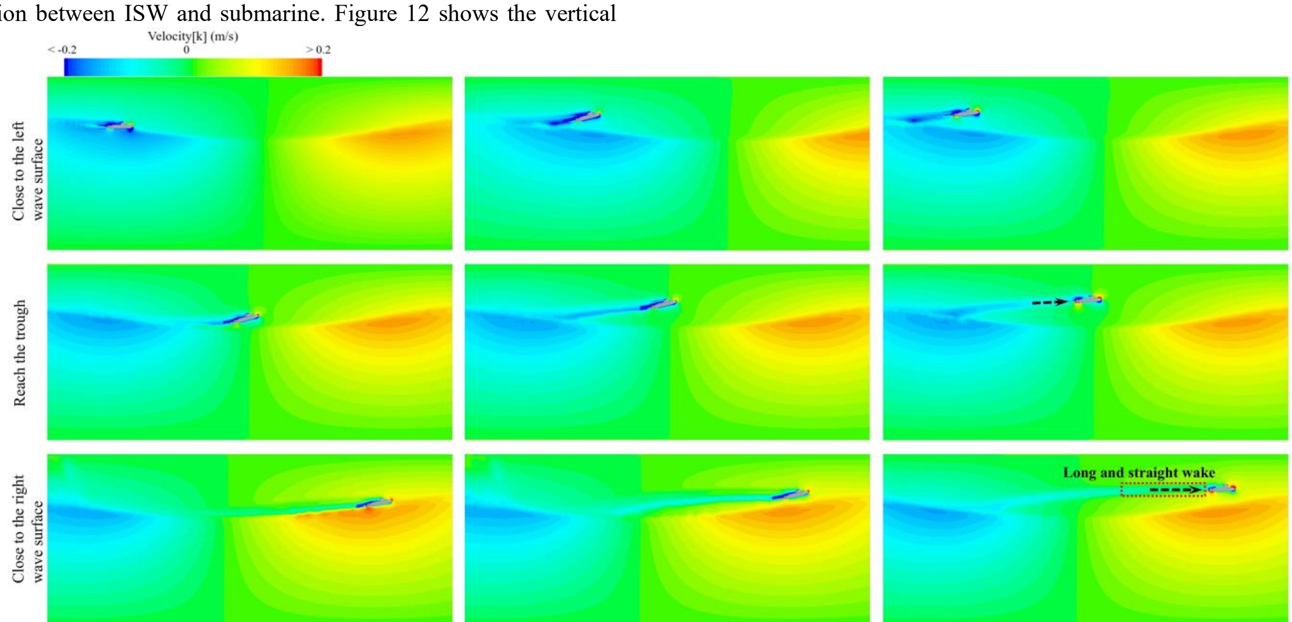

（a） case 1 （b） case 2 （c） case 3

Fig. 12 Vertical velocity field at three representative stages of ISW–submarine interaction.

As observed in Fig. 12, on the left side of the wave crest, the flow field is predominantly blue, indicating a pronounced downward motion of water particles, whereas on the right side of the wave crest, the flow gradually turns yellow, representing the upward recovery of the water particles. In Case 1, owing to the absence of active control, the submarine follows the motion of the surrounding water particles, sinking first and then rising. In Case 2, although stern rudder control is applied and the sinking depth is reduced compared with Case 1, the horizontal velocity of the submarine decreases significantly, as indicated by the previous analysis of the horizontal velocity field. Consequently, the stern rudder is unable to generate sufficient vertical lift to restore the submarine to its initial depth. In contrast, the long and straight wake trailing behind the submarine in Case 3 indicates that the vehicle maintains a high degree of independence from the wave-induced flow, rather than passively drifting with it. The results in Fig. 13 indicate that, in the uncontrolled condition, Case 1 exhibits the most pronounced fluctuations in vertical velocity. Upon entering the internal solitary wave, the maximum sinking velocity reaches 0.21 m/s, while after leaving the wave trough region, the maximum upward velocity attains 0.23 m/s. With the introduction of PD-controlled stern rudder actuation, Case 2 achieves a certain degree of suppression of the initial sinking motion, reducing the peak sinking velocity to 0.076 m/s. Notably, a pronounced upward velocity occurs around t = 162 s, with a peak value of 0.18 m/s. Case 3 demonstrates superior vertical stability, with the smoothest vertical velocity profile among the three cases. The fluctuation amplitude throughout the entire process is strictly confined within ±0.05 m/s.

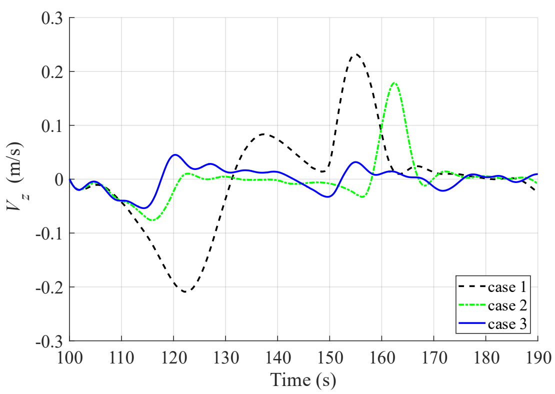

Fig. 13 Horizontal velocity of the submarine.

The Effect of the Controller

This section examines the roles of the PD-controlled stern rudder angle and the PI-regulated propeller rotational speed in suppressing the depth loss of the submarine after encountering an internal solitary wave. The time histories of the stern rudder angle and the corresponding lift force under the three control conditions are presented in Fig. 14.

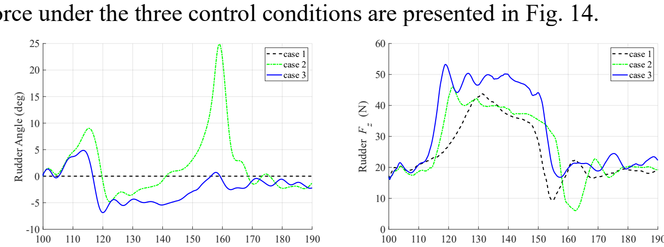

(a) Rudder angle (b) Lift of rudder

Fig. 14 Time histories of the rudder angle and lift.

As shown in Fig. 14, when the stern rudder angle is controlled under a fixed propeller rotational speed (Case 2), the PD controller continuously increases the rudder deflection in order to generate sufficient lift due to the significant loss of forward speed, with the rudder angle reaching a peak value of 25°. In contrast, in Case 3, the rudder angle variation remains very limited throughout the entire disturbance rejection process, staying within the range of −7° to 5°. This indicates that the control system retains a substantial control margin. Meanwhile, the lift generated by the rudder in Case 3 is even greater than that in Case 2, demonstrating a highly efficient control strategy with enhanced effectiveness.

The time histories of the propeller rotational speed and the vertical component of the generated thrust are shown in Fig. 15. As can be observed from the figure, the PI controller substantially increases the propeller rotational speed while the submarine traverses the internal solitary wave. Meanwhile, owing to the submarine's pitch angle, the thrust generated by the propeller attains a peak vertical component of 21.2 N at t = 120 s, which plays a crucial role in preventing depth loss during the initial stage of the encounter.

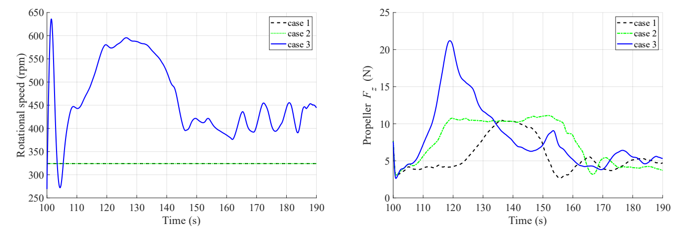

(a) Propeller rotational speed (b) Vertical thrust

Fig. 15 Time histories of rotational speed and vertical thrust.

CONCLUSIONS

This study developed a numerical wave tank based on the eKdV equation to examine the motion behavior and control approaches of a self-propelled Joubert BB2 submarine encountering an ISW, where the initial submergence depth of the submarine is located at the density interface and the cruising speed is set to 1.2 m/s. Overset and sliding mesh techniques were employed to achieve full coupling of hull motion, propeller rotation, and rudder control surface deflection. A hybrid control strategy was proposed, combining PD control for the stern planes and PI control for propeller speed. Its effectiveness was compared with both the uncontrolled case and the rudder-only control case. The main conclusions are as follows:

(1) When no control is applied, the self-propelled submarine suffers considerable depth drop during ISW encounter. With PD control regulating stern plane deflection, the depth drop is reduced to 33% of the uncontrolled magnitude. Incorporating PI control to dynamically adjust propeller speed further lowers the depth loss to 17%.

(2) When only PD control is applied to the stern planes, the reverse horizontal flow field of the ISW causes a notable reduction in submarine forward speed, which in turn diminishes control surface effectiveness. Consequently, the stern plane deflection must increase to 25° to generate sufficient lift and prevent further depth drop.

(3) Under the combined PI (propeller rotational speed) and PD (stern rudder) control strategy, the submarine sustains its advance speed at the target value of 1.2 m/s, preserving high rudder authority. This allows sufficient hydrodynamic lift to be produced with a maximum stern plane angle of only 7°. Moreover, the vertical thrust component from the propeller contributes to upward motion. The complementary interaction of rudder lift and propeller thrust results in swift recovery to the original depth.

ACKNOWLEDGEMENTS

This work is supported by the National Natural Science Foundation of China (Grant Nos. 52571360, 52131102), to which the authors are most grateful.

REFERENCES

Alford, MH, Peacock, T, MacKinnon, JA, Nash, JD, Buijsman, MC, Centurioni, LR, and Tang, TY (2015). "The formation and fate of internal waves in the South China Sea," *Nature*, 521(7550), 65–69.

Benjamin, TB (1966). "Internal waves of finite amplitude and permanent form," *J Fluid Mech*, 25(2), 241–270.

Cai, S, Long, X, and Gan, Z (2003). "A method to estimate the forces exerted by internal solitons on cylindrical piles," *Ocean Eng*, 30(5), 673–689.

Cai, S, Wang, S, and Long, X (2006). "A simple estimation of the force exerted by internal solitons on cylindrical piles," *Ocean Eng*, 33(7), 974–980.

Cai, S, Long, X, and Wang, S (2008). "Forces and torques exerted by internal solitons in shear flows on cylindrical piles," *Appl Ocean Res*, 30(1), 72–77.

Cao, L, Pan, Y, Gao, G, Li, L, and Wan, D (2024). "Review on the hydro- and thermo-dynamic wakes of underwater vehicles in linearly stratified fluid," *J Mar Sci Eng*, 12(3), 490.

Carrica, PM, Kim, Y, and Martin, JE (2019). "Near-surface self propulsion of a generic submarine in calm water and waves," *Ocean Eng*, 183, 87–105.

Celik, IB, Ghia, U, Roache, PJ, Freitas, CJ, Coleman, H, and Raad, P.E. (2008). "Procedure for estimation and reporting of uncertainty due to discretization in CFD applications," *J Fluids Eng*, 130(7), 078001.

Chen, M, Zhang, N, Zheng, W, and Li, Y (2023). "Numerical simulation of near-surface turn maneuver of a generic submarine," *Ocean Eng*, 287, 115835.

Cheng, L, Du, P, Hu, H, Xie, ZL, Yuan, Z, Kaidi, S, Chen, X, Xie, L, Huang, X, and Wen, J (2023). "Control of underwater suspended vehicle to avoid 'falling deep' under the influence of internal solitary waves," *Ships Offshore Struct*, 19(9), 1349–1367.

Cheng, L, Du, P, Wang, C, Xie, ZL, Hu, HB, Chen, XP, Li, ZY, and Yuan, ZM (2024a). "Tuning control parameters of underwater vehicle to minimize the influence of internal solitary waves," *Ocean Eng*, 310, 118681.

Cheng, L, Wang, C, Guo, B, Liang, Q, Xie, Z, Yuan, Z, Chen, X, Hu, H, and Du, P (2024b). "Numerical investigation on the interaction between large-scale continuously stratified internal solitary wave and moving submersible," *Appl Ocean Res*, 145, 103938.

Choi, W, and Camassa, R (1999). "Fully nonlinear internal waves in a two-fluid system," *J Fluid Mech*, 396, 1–36.

Cui, J, Dong, S, Wang, Z, Han, X, and Lv, P (2020). "Kinematic response of submerged structures under the action of internal solitary waves," *Ocean Eng*, 196, 106814.

Cui, J, Dong, S, and Wang, Z (2021). "Study on applicability of internal solitary wave theories by theoretical and numerical method," *Appl Ocean Res*, 111, 102629.

Ding, W, Sun, H, Zhao, X, and Ai, C (2023). "Numerical study of the interaction between an internal solitary wave and a submerged extended cylinder using OpenFOAM," *Ocean Eng*, 274, 113985.

Dunphy, M, Subich, C, and Stastna, M (2011). "Spectral methods for internal waves: indistinguishable density profiles and double-humped solitary waves," *Nonlinear Process Geophys*, 18(3), 351–358.

Gong, Y, Xie, J, Xu, J, Chen, Z, He, Y, and Cai, S (2022). "Oceanic internal solitary waves at the Indonesian submarine wreckage site," *Acta Oceanol Sin*, 41(3), 109–113.

Guo, E, Wang, Y, Cao, L, and Wan, D (2024). "Numerical investigation on steady turning motion of a generic submarine near the free surface," *Ocean Eng*, 313, 119375.

Han, K, Cheng, X, Liu, Z, Huang, C, Chang, H, Yao, J, and Tan, K (2021). "Six-DOF CFD simulations of underwater vehicle operating underwater turning maneuvers," *J Mar Sci Eng*, 9(12), 1451.

He, Z, Wu, W, Wang, J, Ding, L, Chang, Q, and Huang, Y (2024). "Investigations into motion responses of suspended submersible in internal solitary wave field," *J Mar Sci Eng*, 12(4), 596.

Helfrich, KR, and Melville, WK (2006). "Long nonlinear internal waves," *Annu Rev Fluid Mech*, 38, 395–425.

Hirt, CW, and Nichols, BD (1981). "Volume of fluid (VOF) method for the dynamics of free boundaries," *J Comput Phys*, 39(1), 201–225.

Huang, M, Gao, C, and Zhang, N (2023). "Numerical research on hydrodynamic characteristics and influence factors of underwater vehicle in internal solitary waves," *Int J Offshore Polar Eng*, 33(1), 27–35.

Lee, CY, and Beardsley, RC (1974). "The generation of long nonlinear internal waves in a weakly stratified shear flow," *J Geophys Res*, 79(3), 453–462.

Lin, Z, and Zan, X (2021). "Numerical study on load characteristics by internal solitary wave on cylinder sections at different depth and its parameterization," *Ocean Eng*, 219, 108343.

Menter, FR (1994). "Two-equation eddy-viscosity turbulence models for engineering applications," *AIAA J*, 32(8), 1598–1605.

Michallet, H, and Barthelemy, E (1998). "Experimental study of interfacial solitary waves," *J Fluid Mech*, 366, 159–177.

Overpelt, B, Nienhuis, B, and Anderson, B (2015). "Free running manoeuvring model tests on a modern generic SSK class submarine (BB2)," *Proc Pacific Int Maritime Conf*, Sydney, MARIN, 1–14.

Wang, SD, Wei, G, Du, H, Wu, JL, and Wang, XL (2020). "Experimental investigation of the wave-flow structure of an oblique internal solitary wave and its force exerted on a slender body," *Ocean Eng*, 201, 107057.

Wei, G, Du, H, Xu, X, Zhang, Y, Qu, Z, Hu, T, and You, Y (2014). "Experimental investigation of the generation of large-amplitude internal solitary wave and its interaction with a submerged slender body," *Sci China Phys Mech Astron*, 57(2), 301–310.

Xuan, P, Du, H, Wang, SD, Peng, P, and Wei, G (2023). "Experimental and theoretical study of internal solitary wave loads on a submerged slender body," *Ocean Eng*, 272, 113936.

Xuan, P, Du, H, Wang, S, Peng, P, and Wei, G (2024). "The applicability of nonlinear theories of the internal solitary wave and its loads on slender body by experimental methods," *Appl Ocean Res*, 153, 104279.

Zan, X, and Lin, Z (2020). "On the applicability of Morison equation to force estimation induced by internal solitary wave on circular cylinder," *Ocean Eng*, 198, 106966.

Zhao, BB, Ertekin, RC, Duan, WY, and Webster, WC (2016). "New internal-wave model in a two-layer fluid," *J Waterw Port Coast Ocean Eng*, 142(3), 04015022.